Investigating Two-Step $MAPbI_3$ Thin Film Formation during Spin Coating by Simultaneous in Situ Absorption and Photoluminescence Spectroscopy

Mihirsinh Chauhan,[1,2,#] Yu Zhong,[1,3,#] Konstantin Schötz,[1] Brijesh Tripathi,[2] Anna Köhler,[1,4] Sven Huettner,[3] Fabian Panzer[1*]

1: Soft Matter Optoelectronics, University of Bayreuth, 95440 Bayreuth, Germany

2: School of Technology, Pandit Deendayal Petroleum University, 382007 Gandhinagar, India

3: Department of Chemistry, University of Bayreuth, 95440 Bayreuth, Germany

4: Bayreuth Institute of Macromolecular Research (BIMF) and Bavarian Polymer Institute (BPI), University of Bayreuth, 95440 Bayreuth, Germany.

#: Authors contributed equally

Corresponding Author: fabian.panzer@uni-bayreuth.de

Keywords: two step method, crystallization, halide perovskite, hybrid perovskite

Abstract

Until today, the two-step processing method represents an attractive route for the thin film formation of halide perovskites. However, a fundamental understanding about the film formation dynamics in case of spin coating methylammonium iodide (MAI) on PbI_2 has not been established yet. Here we apply in-situ optical spectroscopy during the two-step film formation of the model halide perovskite $MAPbI_3$ via spin coating. We identify and analyze in detail the optical features that occur in photoluminescence and corresponding absorption spectra during processing. We find that the film formation takes place in five consecutive steps, including the formation of a $MAPbI_3$ capping layer via an interface crystallization and the occurrence of an intense dissolution-recrystallization process. Consideration of confinement and self-absorption effects in the PL spectra, together with consideration of the corresponding absorption spectra allows to quantify the growth rate of the initial interface crystallization to be 11 nm/s for our processing conditions. We find the main dissolution recrystallization process to happen with a rate of 445 nm/s, emphasizing its importance to the overall processing.

TOC:

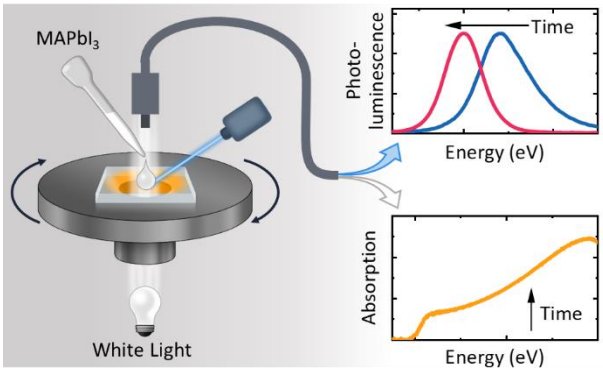

1. Introduction

The ongoing increase in the efficiencies of perovskite-based optoelectronic devices, in particular solar cells, has been delighting the research community for several years now. Key aspects for this development were various breakthroughs in the thin film processing of the perovskite layer. One of the most important solution-based processing approaches to date is the so called two-step method, which was first reported in 2013.[1, 2] In this method, a PbI_2 layer is produced in a first process step, e.g. via spin coating, and then brought into contact with methylammonium iodide (MAI) dissolved in an alcohol, e.g. isopropanol (IPA), in a second processing step, thus initiating the growth of the perovskite $MAPbI_3$. It is possible to realize the second processing step either by exposing the PbI_2 layer to a MAI gas phase, by dipping the PbI_2 layer into a MAI solution, or by spin coating the latter onto the PbI_2 substrate. The main advantage of the two-step method is seen in the supposedly higher process control compared to other processing methods.[3] However, it became clear in the last few years that, similar to other solution-based film processing methods, the final morphological and thus optoelectronic properties sensitively depend on the precise processing conditions also in the case of the two-step method.[4-8] Some studies have investigated the film formation dynamics during the two-step method,[9] and found that the $MAPbI_3$ crystallization process depends e.g. on the MAI concentration,[10, 11] temperature,[11, 12] and the timing of the process steps.[2] Depending on the concrete processing conditions it is possible that different types of crystallization occur, namely in-situ interface transformation or solid liquid recrystallization, or both.[13, 14] So far, most of the knowledge about the crystallization behavior of the two-step method was obtained for the case of dipping the PbI_2 layer in MAI solution, where crystallization takes place on relatively long time scales.[3] In contrast, faster crystallization takes place when applying MAI/IPA via spin-coating, which leads to more homogeneous, compact and smoother films and thus to better solar cells, rendering it the more technology relevant processing strategy.[4] Recently we have developed a measurement setup that allows to measure absorption spectra and, in parallel, photoluminescence (PL) in-situ during solution-based processing of semiconductor materials, such as spin-coating.[15] By investigating the optical properties of halide perovskites, it is possible to extract detailed information about their electronic structure, and concomitantly about their composition.[16-20] Thus, in this work, we use in-situ absorption and simultaneous PL spectroscopy to investigate the film formation dynamics of $MAPbI_3$ for a two-step processing approach using spin coating. We observe

changes in both, absorption and PL during the spin-coating process. This allows us to categorize the film formation process into five different time ranges. By carefully considering quantum confinement and self-absorption effects, we analyze in detail the spectroscopic changes in the different time ranges. This allows associating the changes in the optical properties with specific morphological states. We find that both, interface crystallization, as well as a dissolution-recrystallization process occur. Based on our results it is possible to understand the full sequence of perovskite formation dynamics that occur in the two-step processing via spin coating.

2. Results

In the first processing step we spin coat a solution of PbI_2 in Dimethylformamide (DMF) (461 mg/ml) onto a glass substrate (Figure 1a) and anneal it at 100 °C for 5 minutes (Figure 1b). This leads to a compact PbI_2 thin film. In the second processing step, we drop 200 µl of MAI dissolved in IPA (40 mg/ml) onto the PbI_2 film to induce the $MAPbI_3$ crystallization and immediately start spin coating (corresponding to t=0 s), where the target spin speed of 1000 rpm/min is reached after 2 seconds (Figure 1c). The temperature of sample and MAI solvent during the spin coating is kept at 26 °C. During this second processing step, we monitor the optical properties, i.e. absorption and PL, using a home built spin coater and optical detection system, both described in detail in reference [15]. In brief, the rotating substrate with the solution is excited with a white-light-source pulsed at 11 Hz from underneath the chuck of the spin-coater, through a hole, and its transmission is recorded with a glass fiber cable connected to a spectrograph.

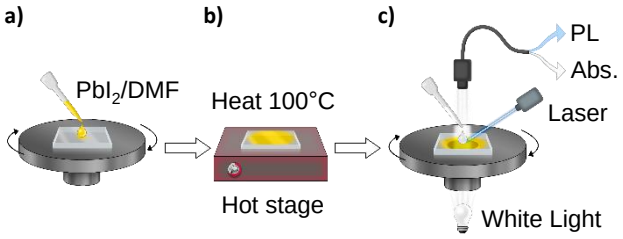

Figure 1: The preparation of $MAPbI_3$ film and the in-situ spectroscopy setup. a) PbI_2 in DMF is spin coated on a glass substrate. b) Heat annealing of the PbI_2 layer. c) MAI in IPA is spin coated on PbI_2 layer and, during spin coating, PL and absorption of the film is detected.

During the off-periods, a laser beam at 520 nm (2.38 eV) excites the sample and the resulting luminescence is recorded using the same glass fiber cable connected to the spectrograph. In this way, pairs of transmission and PL spectra are measured at a rate of 11 pairs per second. To correct the transmission of $MAPbI_3$ $I(t)$ for the transmission of the setup I_0, we also recorded the transmission signal obtained with a quarz substrate and subtracted it such as to obtain the time dependent optical density via $OD(t) = \log(I_0/I(t))$. The resulting spectra is shown in the supporting information (Figure S1). It turns out that a reflection signal from the initially unreacted PbI_2 film obscures the clear identification of the $MAPbI_3$ absorption in particular at early times, when the $MAPbI_3$ signal is still weak. We therefore also recorded the transmission signal obtained from a quartz substrate covered with a PbI_2 film and used this as reference value I_{ref} to calculate the time dependent optical density as $OD(t) = \log\big(I_{ref}/I(t)\big)$ shown in Figure 2a. One may argue that, at later stages, this procedure implies subtracting a no longer existing reflection signal as the PbI_2 layer has been used up. However, once the PbI_2 has been used up, the transmission from the $MAPbI_3$ is sufficiently strong so that this small subtraction has essentially no effect. All spectra are also set to a common baseline to account for fluctuations in optical scattering. Figure 2 shows the evolution of the absorption spectra (Figure 2a) and of the corresponding PL spectra (Figure 2b), where each PL spectrum is normalized to its maximum value. They are both plotted as 2D color maps, so that the color indicates the intensity of PL or optical density (OD). For reference and visualization, the absorption and PL spectrum at 14 s is indicated at the side of the maps.

From Figure 2a it becomes clear that little absorption evolves within the first 12 seconds of processing, whereas the main increase in absorption intensity occurs between 12 – 14 s. From about 14 s onwards, the absorption remains largely unaltered. We point out that the absorption cannot be evaluated quantitatively within the first 4 s, since until then the pipette, used to distribute the MAI solution across the glass substrate at the beginning of spin coating, was in the beam path. In contrast to the absorption, a photoluminescence peak prevails over the entire time range investigated (Figure 2b). Its energetic position and width changes in the first 14 seconds and remains constant thereafter. It is noteworthy that this PL has a finite intensity even when there is only very little absorption from the $MAPbI_3$, implying a high quantum yield compared to later times, when there is significant $MaPbI_3$ absorption. For reference, a plot of the PL spectra with absolute intensities, is given in the supporting information (Figure S1).

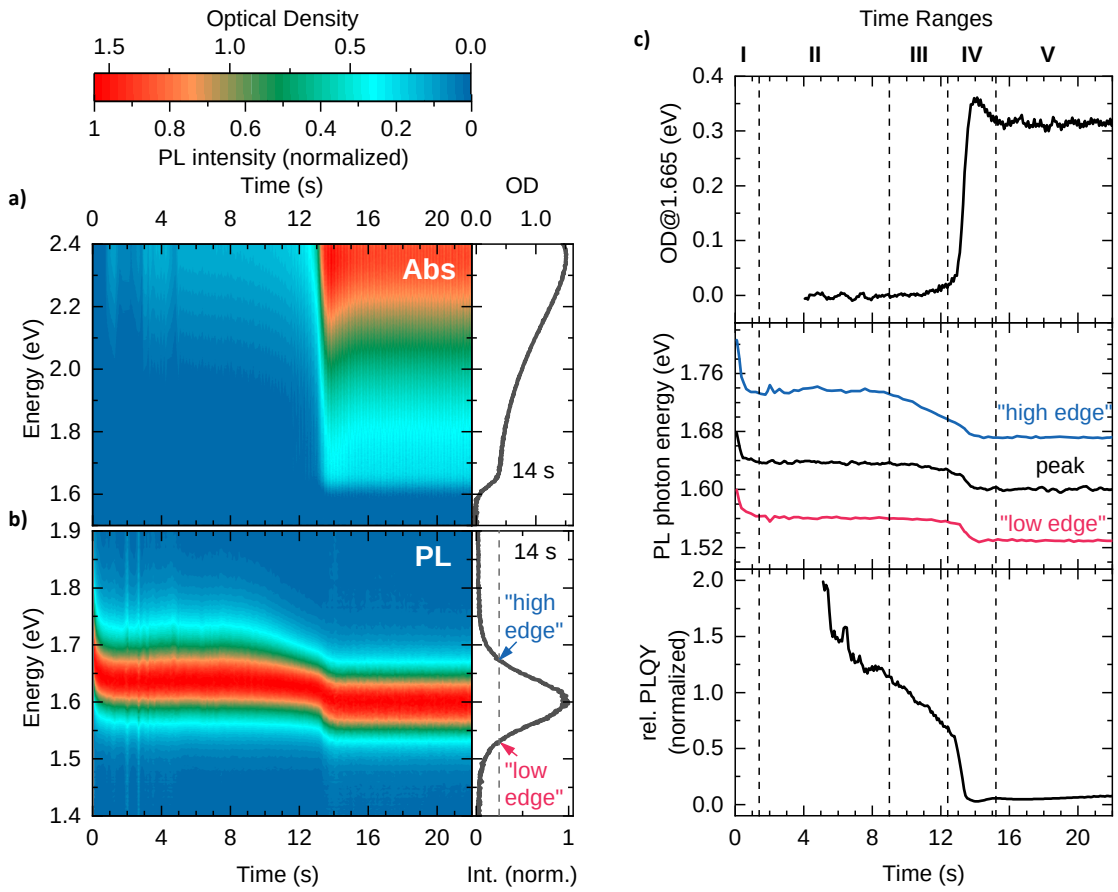

Figure 2: a) 2D Absorption map. The colour indicates the optical density b) PL map, with every spectrum being normalized. c) Evolution of (top panel) the optical density at 1.665 eV, (middle panel) the PL at the positions of the peak, "high edge" and "low edge", and (bottom panel) of the PLQY relative to the value at 10 s.

To analyze the different spectroscopic signatures and temporal changes in more detail, we display the temporal evolution of different spectral features in Figure 2c. The optical density at 1.665 eV, indicates how the $MAPbI_3$ absorption develops with time. We also show the evolution of the PL peak position and the two photon energies at which the PL has dropped to 25% of its maximum intensity (essentially following, the turquoise line in Figure 2b). This is referred to as "high edge" and "low edge". Further, the temporal evolution of the integrated PL intensity, corrected for the concomitant changes of the absorption at the laser excitation wavelength (2.38 eV) normalized to the value after 10 seconds, is shown. This indicates the relative change of the PL quantum yield (PLQY).

If we take a closer look at the time evolution of the optical parameters described above (Figure 2c), we can identify five consecutive time ranges between which specific spectral

changes of PL or absorption occur. We briefly describe what characterizes these different regimes, before analyzing each regime in detail. In the first time range, i.e. the first 1.4 seconds, indicated as I in Figure 2c, we observe photoluminescence, and its spectrum shows a fast initial shift towards lower energies. In the subsequent time range II, i.e. the next 8 seconds, the PL shape remains constant, while there is no noticeable change in absorption intensity from 4 s onwards. In time range III, the absorption increases slightly, and there are spectral changes in the PL. The high-energy edge of the PL shifts to lower energies, while the position of the low-energy edge remains constant. Range IV can be associated with the steep increase and subsequent decreases in absorption. Simultaneously a further shift of the whole PL spectrum to lower energies occurs, accompanied by a significant reduction of the relative PLQY. After that, in range V, no further change in the absorbance and PL occur.

Range I: As mentioned above, absorption in range I cannot be evaluated. However, directly after applying the MAI solution to the PbI_2 layer, an initial PL spectrum with a maximum at 1.68 eV occurs, which shifts within the first 1.4 seconds by about 50 meV to lower energies (Figure 3a top). Figure 3b shows the temporal evolution of the energetic position of the PL peak, together with a fit to an exponential decay that gives a time constant of 0.23±0.05 s. We note that the spectral shape of the PL peak is not symmetrical. Rather, it shows a high energy tail that becomes particularly obvious when fitting a hyperbolic secant, e.g. to the spectrum at 1.4 s (Figure S2). Such a lineshape was previously found to account well for thermal and inhomogeneous broadening of the PL peak shape of halide perovskites.[21]

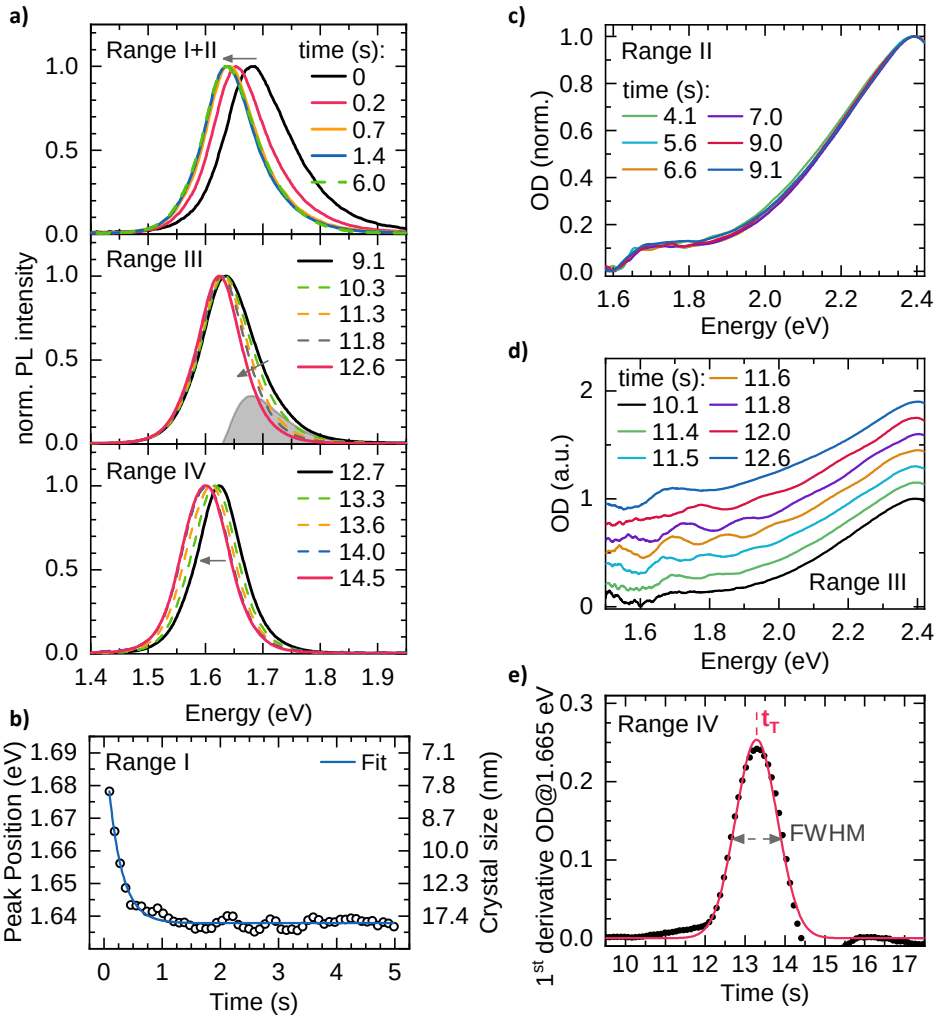

Figure 3: a) Evolution of PL during processing. Top: Normalized PL within the first 1.4 s (Range I) and at 6.0 s (Range II). Middle: Normalized PL from 9.1 s (black line) to 12.6 s (red line) (Range III). The difference between the spectra at 9.1 s and 12.6 s is shown in grey. Bottom: Normalized PL from 12.7 s to 14.5 s (Range IV). b) Temporal evolution of the PL peak position together with an exponential decay fit. Also the crystal size that corresponds to a certain PL peak position, as described in the text, is given. c) Normalized absorption spectra between 4.1 s (red) to 9.1 s of processing (Range II). d) Absorption spectra from 10.1 s to 12.6 s (Range III). For clarity each spectrum is offset by 0.15. e) The 1st derivative of OD at 1.665 eV together with a fit of a Gaussian. The peak position is defined as transition time t_T.

To further investigate what may give rise to the high-energy PL tail and the initially blue-shifted position of the maximum, we recall that PL spectra that were blue shifted compared to their bulk PL have been repeatedly associated in the past to a confinement effect of the excited state by a finite crystallite size.[22-25] For $MAPbI_3$, this effect occurs for crystallite- or grain sizes

below approximately 25-30 nm.[26-28] We follow the approach outlined by Parrott et al. to correlate the measured PL peak position with the crystal size,[27] via

$$E = E_g + b/d^2 \quad (1)$$

where E_g corresponds to the band gap energy, which we set to 1.63 eV. The parameter b represents a constant, which in literature is found to be in the range between 1 – 5 eV nm^2 for $MAPbI_3$,[27, 29] so that we assume a value of 3 eV nm^2 (see SI for more details). With the help of Equation 1, the evolution of peak position with time translates into an evolution of film thickness with time (Figure 3b and Figure S3). It appears that the film formation starts at a thickness of about 8 nm, increases to about 20 nm within the first 1.5 s, and then remains constant. A fit to the evolution of crystal size in the range up to 1.0 s gives an initial $MAPbI_3$ growth rate for the film thickness in the range of 11±2 nm/s (Figure S3).

Range II: The measured absorption spectra between 4.1 and 9.1 s in range II correspond to the known $MAPbI_3$ absorption spectrum and its shape remains constant over time (Figure 3c). After the initial spectral changes in time range I, the shape of the PL spectrum stabilizes from about 1.5 s onwards. This defines the beginning of range II. The PL shape remains nearly constant until a processing time of 9.1 s.

Range III: While the shape of the absorption spectrum does not change over time at the beginning of range III, we observe a modulation of the measured spectra in the time range between 11.4 s and 12.6 s (Figure 3d). These can be associated with a thin film interference effect, which is often used to optically determine the thickness of thin films.[30] The layer thickness *d* can be calculated from the spectral position of the extrema via,[31, 32]

$$d = \frac{\lambda_1 \lambda_2}{2(\lambda_1 n_2 - \lambda_2 n_1)} \quad (2)$$

where λ_1 and λ_2 correspond to the wavelengths of two adjacent maxima or minima and n_1, n_2 represent the refractive index of the layer material at λ_1 and λ_2. While the determination of λ_1 and λ_2 is relatively easily accessible from the measured spectra (see Figure S7 for details), it is not so obvious which material causes the thin film interference in range III. If the thicknesses are calculated using the refractive indices for $MAPbI_3$ (~2.4-2.5) or PbI_2 (~3.1-3.2), the resulting values are clearly too high compared to the thicknesses determined based on the absorption and profilometer data (see SI for details). If the refractive indices of isopropanol (~1.3-1.4) are used, we obtain a thickness of 3.6 µm at 11.4 s, which is rapidly decreasing to 1.4 µm at 12.6 s.

From 9.1 s onward, the spectral shape of the PL evolves. The high-energy edge shifts from 1.74 eV at 9.1 s to 1.70 eV at 12.6 s, i.e. by about 40 meV. In the same time range, the spectral position of the low edge shifts merely by 7 meV, starting from 1.56 eV, (Figure 2b,c and Figure 3a middle panel). This spectral dynamic results in an asymmetric narrowing of the measured PL peak from the high-energy edge. At first sight, this might be interpreted as self-absorption effect in which the PL intensity reduces in the spectral overlap region of PL and absorption.[33] To check the plausibility of the self-absorption scenario in time range III, we used the PL spectrum at the beginning of range III (i.e. at 9.1 s) as the reference spectrum to calculate the absorption edge using the subsequent PL spectra (see Figure S4). This is a well-known approach, especially for the optical investigation of inorganic semiconductors, where information about the absorption edge can be obtained based on PL data.[34, 35] However, we find that the absorption edges determined by this approach do not match well with the absorption edges determined by the optical density measurements in terms of both shape and energetic position (Figure S4). To assess the influence of self-absorption on the PL more precisely, we analyzed the PL spectra in range III using a quantitative model we already successfully used in the past for this purpose.[36] An important feature of this model is that it takes into account extended optical paths in the material due to internal reflections at the layer interfaces. We find that in realistic and exaggerated scenarios with regard to assumed layer thicknesses and or boundary layer properties, it is virtually impossible to model the experimentally observed narrowing of only one PL edge (Figure S5). Rather, a spectral shift of the entire spectrum would result from an increasing amount of self-absorption, which also agrees with other literature reports.[27 36] From the absorption data in range III we further observe that the absorption is relatively low (OD < 0.01 at 1.67 eV), which is further in agreement with the notion that a significant self-absorption effect in time range III is absent.[27, 37]

However, it is noticeable that at the end of range III the PL peak appears more symmetrical, compared to its spectral shape at the beginning of range III. The difference spectrum calculated from the PL spectra at 9.1 s and 12.6 s (shaded area in Figure 3a middle panel) peaks at 1.68 eV. This matches with the peak position of the first measured PL spectrum at 0 s. If we also calculate the difference spectra between the PL spectrum at 9.1 s and the other spectra in range III, they result in essentially the same spectral shape with peak position at 1.68 eV (Figure S6). It is important to note that this difference spectrum does not shift to the

red with increasing time. Rather, exactly the same spectrum prevails at all times, yet its intensity reduces. Thus, the spectral changes in range III can also be understood as decreasing intensity of an additional higher energetic PL feature, which finally disappears at the end of range III.

Given the spectral coincidence of the additional high-energy PL feature with the PL at early times, it is straightforward to attribute this feature to small crystallites where the exciton wavefunction is still confined and thus the transition is blue-shifted. Using Equation 1, the peak position of the difference PL at 1.68 eV would correspond to a crystal size of about 15 nm.

Range IV: The significant increase in absorption between 12.6 and 14.0 s is the most noticeable spectral change in range IV (Figure 2a). To quantify this increase more precisely, it is advantageous to calculate the derivative of the time-dependent OD at 1.665 eV, which leads to a peak shape.[38] By fitting a Gaussian to this peak, we can quantify the transition time t_T from the maximum. The full width half maximum (FWHM) gives information about the width of the transition (Figure 3e). We find t_T= 13.3 s and FWHM=1.2 s.

The increase in absorption can be associated with an increase in film thickness. To this end, we used the absorption coefficient of $MAPbI_3$ from literature,[39] to convert the time-dependent (offset corrected) optical density from Figure 2c in the energy range between 1.6 eV and 1.7 eV into a time-dependent layer thickness, shown as black circles in Figure 4 (see also Figure S8 for details). The steep increase in the absorption spectrum then corresponds to an increase of layer thickness from about 50 nm at the beginning to about 500 nm at the end of range IV. If we approximate this evolution by a linear fit in the range between 13 to 14 s, this results in a growth rate of 445±15 nm/s (Figure S9). Also indicated in Figure 4 is the film thickness that results from fitting the interference pattern in range III using the refractive index of isopropanol (orange diamonds), and the film thickness that is obtained at early times from fitting the shift in the PL spectra by Equation 1 (red squares).

Simultaneously to the steep increase in absorption, the entire PL spectrum shifts from 1.63 eV to 1.60 eV (see Figure 2c and Figure 3a bottom). If we assume that this shift is due to self-absorption, we can derive the associated film thickness that causes such an absorption. We did this, using a modelling approach that considers multiple reflections and that is detailed in Ref. [36]. As detailed in the Supporting information (Figure 10), we start by using the PL spectrum at 12.7 s, i.e. at the beginning of range IV, and consider the intensity of $MAPbI_3$ absorption present in that moment to calculate the PL spectrum that would result in the absence of self-

absorption. The spectrum calculated in this way peaks at 1.63 eV, matching well with the measured PL spectrum after 1.4 s (end of range I), which confirms our approach. As next step, we calculated the layer thickness necessary to modify this PL spectrum in such a way that it matches the measured PL spectra at each time in range IV (Figure S11). The thicknesses that we obtain by this approach are indicated as green triangles in Figure 4. From the good agreement with the layer thicknesses obtained from considering the OD we conclude that our approach is correct, i.e. the shape of the PL spectra in range IV is indeed the result of self-absorption from the increasing amount of $MAPbI_3$.

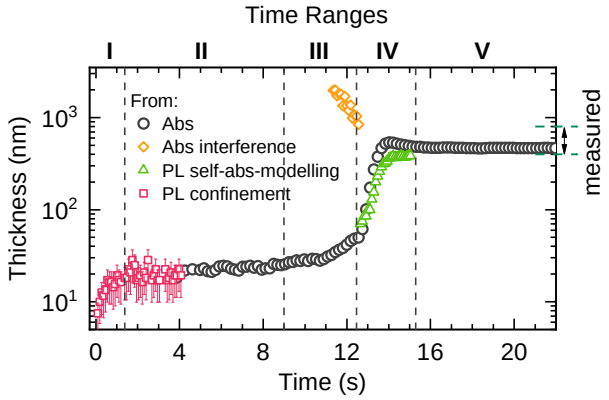

Figure 4: The film thickness as a function of spin-coating time, derived with different approaches as detailed in the text. Black circles: derived by converting OD into thickness, orange diamonds: derived by fitting interference pattern, red squares: derived by associating a PL shift with confinement effects, green triangles: derived by associating the PL shift with self-absorption of differently thick films.

Range V: The last time range, starting from 14.0 s, is characterized by the fact that there are no temporal changes in both absorption and PL, i.e. the film formation is complete. X-ray scattering results reveal that after time range V no PbI_2 exists in the film, suggesting a full conversion to $MAPbI_3$ (Figure S12). The layer thickness extracted using the absorption data is approximately 500 nm in range V, which matches well with the layer thickness range from 400 to 800 nm determined using a profilometer (Figure 4). SEM images of a final film show a compact surface coverage and grain sizes in the range from 50 to 300 nm (Figure S13). While the relative PLQY has decreased significantly, the PL spectrum appears symmetric, suggesting that no additional PL signatures are present at the end of the processing.

3. Discussion

Having analyzed the spectral features in detail, we can now proceed to derive a possible model for the successive film formation. As before, we shall consider the different temporal regimes one after another. The overall picture we suggest is summarized in Figure 5.

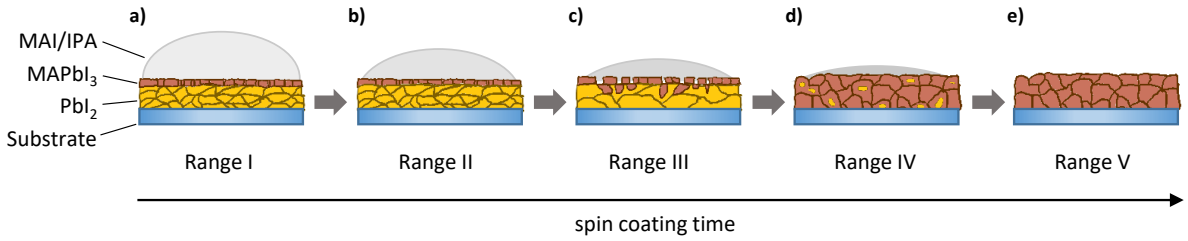

Figure 5: a) Range I: The formation of a $MAPbI_3$ capping layer. b) Range II: Further concentration of the MAI solution above the capping layer through evaporation in the course of several seconds, while the capping layer prevents further $MAPbI_3$ crystallization. c) Range III: The iodine concentration increases because of the solvent evaporation and leads to the beginning of the dissolution of $MAPbI_3$ capping layer. d) Range IV: Fast dissolution-recrystallization process, when most $MAPbI_3$ forms. e) Range V: All PbI_2 is transferred into $MAPbI_3$ and a stable state is reached.

Range I: The analysis of the PL spectra suggested the initial formation of small $MAPbI_3$ crystals with crystal sizes that confine the wavefunction below about 25 nm, immediately after applying the MAI solution on the PbI_2 layer. As suggested by the PL shift to lower energies, these crystallites grow fast with a growth rate of 11 nm/s to sizes above about 25 nm in the course of range I. The good match of the calculated crystal sizes from the confinement effect at the end of range I and the thickness extracted from the first reliable absorption spectra in range II of about 20 nm confirm our approach.

Fu et al. reported the initial formation of a $MAPbI_3$ capping layer when dipping PbI_2 layers into MAI / IPA solution, for concentrations above 10 mg/ml.[13] The formation of this capping layer was also found to happen faster for higher concentrations, while the average grain size decreases.[11, 13] The MAI concentration of 40 mg/ml used in our study is well above 10 mg/ml, so that we associate the initial occurrence of PL and its rapid shift to lower energies as the spectroscopic signatures of the initial formation of $MAPbI_3$ crystallites that grow within range I such as to form a capping layer. This is also in agreement with the results from Schlipf et al. who investigated the $MAPbI_3$ two-step conversion process with time resolved scattering methods and find a laterally confined crystal growth at the beginning of the crystallization.[40]

Ko et al. reported that the growth rate of the $MAPbI_3$ nuclei is independent from the MAI concentration, investigating a range between 4 – 8 mg/ml.[11] Their results on the evolution of grain size suggest a growth rate in the range between 10-20 nm/s, which agrees very well with the value of 11 nm/s that we find in range I using a concentration of 40 mg/ml. This suggests that the growth rate of $MAPbI_3$ nuclei in the two-step process at ambient conditions remains mainly unchanged over at least an order of magnitude in MAI concentration.

The asymmetric shape of the PL spectrum at the end of range I indicates that after the initial $MAPbI_3$ crystallization, crystallites exist with grain sizes below the confinement limit, i.e. below about 25 nm. Ahn et al. derived a direct correlation between the MAI concentration and the resulting $MAPbI_3$ grain size in case of the two step method.[12, 41] In this framework, a MAI concentration of 40 mg/ml (0.25M) as used in our study transfers to an average grain size of approximately 50 nm (Figure S14), i.e. only slightly higher than the typical confinement limit of $MAPbI_3$.[26-28] As the grain in polycrystalline perovskite thin films typically exhibit a size distribution, it appears reasonable that a certain fraction of grains are below 50 nm so that a confinement effect follows.

Range II: After the formation of the initial capping layer, the lack of evolution in the spectra suggests that the morphology of the buried PbI_2 and of the $MAPbI_3$ capping layer formed in the initial period remains highly stable in time range II. This is consistent with reports where the capping layer was found to be very dense due to the higher density of PbI_2 compared to $MAPbI_3$.[42] As a consequence this has been shown to prevent MAI diffusion to the underlying PbI_2 and thus suppresses further $MAPbI_3$ crystallization.[13]

Range III: The formation of a dense $MAPbI_3$ capping layer in time range II, obviously raises the question how the $MAPbI_3$ crystallization is then to proceed eventually. Here a key observation is that in time range III, the high-energy PL tail reduces with time. Importantly, this did not occur by a gradual red-shift of the blue tail, but by a gradual reduction of the PL spectrum that is associated with small crystallites of about 15 nm and below. The disappearance of these smaller crystallites suggest a dissolution process, similar to that observed when dipping PbI_2 layers in MAI solution.[13, 43] Such a so-called “dissolution-recrystallization-process” or "solid-liquid-recrystallization” is described by the reaction

$$CH_3NH_3PbI_3(s) + I^-(sol) \underset{recystallization}{\overset{dissolution}{\rightleftharpoons}} CH_3NH_3{}^+(sol) + PbI_4{}^{2-}(sol) \qquad (3)$$

In this reaction, the balance is shifted to the right side and the formation of PbI_4^{2-} complexes becomes more likely when the MAI concentration is sufficiently high. This explains, why the process only sets in after a certain time – in our case after 9 s -, when sufficient solvent has evaporated. The generated PbI_4^{2-} complexes are known to dissolve existing $MAPbI_3$, e.g. the capping layer, so that the underlying PbI_2 becomes accessible for the further $MAPbI_3$ crystallization.[13] The dissolution process is considered to start preferably at the grain boundaries and smallest grains,[6, 11, 44] and has also been suggested to take place in the case of two-step processing by spin coating.[44] Consequently, we associate our observed disappearance of the small crystallites with their dissolution in the framework of the dissolution-recrystallization process that sets in during time range III. Even though the smaller $MAPbI_3$ crystallites dissolve, we do not observe a reduction of absorption, but even a slight increase of the $MAPbI_3$ thickness from 25 to 50 nm within range III. This suggests that in parallel to the dissolution of the smaller crystallites, the underlying PbI_2 reacts with MAI to form further $MAPbI_3$ which overcompensates the loss from the dissolution process. Obviously, the newly formed $MAPbI_3$ does not occupy the space of the just dissolved $MAPbI_3$, but rather deposits add existing larger $MAPbI_3$ crystallites, similar to an Ostwald ripening process.

The occurrence of thin film interference in the absorption spectra in range III is consistent with the notion of a dissolution-recrystallization process. It is conceivable that the interference stems from the MAI/IPA solution layer, possibly influenced by a deterioration of the layer coverage due to the dissolution process. However, it is not clear to which extent the PbI_4^{2-} interacts with the MAI/IPA solution, from which a change in refractive index might occur. In such a case, we expect an increase of the refractive index of the solution layer, as lead halide systems typically exhibit a higher refractive index compared to IPA. Thus, the layer thickness obtained based on the refractive index values of IPA in Figure 4 represents an upper limit. Further, more detailed investigations are needed to fully address this aspect in the future.

Ranges IV and V: Further solvent evaporation rapidly increases the local MAI concentration and thus further accelerates the solid solution recrystallization process in time range IV. The steep increase of absorption suggests that the equilibrium in Equation 3 shifts significantly towards the recrystallization process. The time scale for the main dissolution-recrystallization process of 1.2 s that we obtained from Figure 3e is significantly shorter than the typical time scales for this process in the case of dipping the PbI_2 in MAI/IPA solution.[6] Similarly, the growth rate of 445±15 nm/s for the recrystallization process in range IV is much higher than the

growth rate of the $MAPbI_3$ capping layer in range I. This could also explain the significant decrease of the PLQY within range IV, where the fast recrystallization leads to an increased defect density and thus to a more pronounced non-radiative PL decay. The grain sizes of a final film exceed 50 nm as determined by SEM (Figure S13). This agrees well with the symmetric shape of the PL spectrum and suggests that no more grains with sizes below 25 nm are present. The spectral position of the PL also matches with the expected bulk spectrum when accounting for self-absorption.

4. Summary and Conclusion

Overall, we have monitored the complete two-step film forming process of $MAPbI_3$ by spin coating using optical spectroscopy. By analyzing the changes in the absorption and photoluminescence spectra, we could identify and quantify different steps in the film formation process. We found that film formation takes place in five consecutive steps, which are (I) the initial formation of a $MAPbI_3$ capping layer, (II) further concentration of the MAI solution above the capping layer through evaporation in the course of several seconds, while the capping layer prevents further $MAPbI_3$ crystallization (III) the beginning of the dissolution of the $MAPbI_3$ capping layer due to the increased iodine concentration in the course of progressing solvent evaporation, (IV) a rapid main dissolution-recrystallization process, during which most of $MAPbI_3$ crystallizes, (V) the final, fully converted, temporally stable state. Consideration of confinement and self-absorption effects in the PL spectra, together with consideration of the corresponding absorption spectra made it possible to quantify the growth rate of the initial interface crystallization to be 11 nm/s and the main dissolution recrystallization process to be 445 nm/s for our experimental conditions. While the rate for the initial interface crystallization is comparable with results from the two-step method via dipping, the growth rate of the dissolution-recrystallization process is significantly higher. This is attributed to the high MAI concentration at the end of the solvent evaporation process. Since most $MAPbI_3$ forms in this short time span (range IV), our results demonstrate the importance of controlling the dissolution-recrystallization process during spin-coating, e.g. by controlling the solvent evaporation rate.

We note that the film formation dynamics, i.e. extend and timings of the interface crystallization and the dissolution-recrystallization process depend on the morphology of the PbI_2 layer, which for example can differ significantly when processed on either a mesoscopic

or a planar TiO_2 underlying layer.[3] Also, for other two-step processing approaches, solvate states can occur which also impact the reaction pathways and crystallization kinetics.[45, 46]

Our work also demonstrates how the film formation process of halide perovskites can be investigated with the help of technically easily accessible in-situ optical spectroscopy and its analysis. This approach can be easily applied to other, more complex perovskite material systems with mixed halide and/or A-site-cations and processing methods in the future. Our work will therefore help to better understand and optimize the film formation process of halide perovskites in general.

5. Experimental Section

Materials and thin film processing:

Lead iodide (PbI_2) beads, N,N-Dimethylformamide (DMF), Isopropanol (IPA) were purchased from Sigma Aldrich Company. Methylammonium iodide (MAI) was purchased from Dyesol company. 461 mg/ml (1M) PbI_2 was dissolved in dimethylformamide (DMF) and heated at 75 ^oC overnight. 40 uL PbI_2 solvent was spin coated on a glass substrate in a N_2 glovebox at 3000 rpm/min for 50 s, followed by annealing at 100 ^oC for 5 min. After that, the PbI_2 film was moved to an ambient atmosphere with the humidity of ~50%. MAI solvent was prepared in IPA in the concentration of 40 mg/ml (0.25M). The PbI_2 film was placed in a homemade spin coater. 200 uL MAI solvent was dropped on the PbI_2 film and immediately spin coated at 1200 rpm/min.

In situ optical spectroscopy:

For transmission measurements, a white LED is placed below the rotating chuck, with a bore along the rotation axis of the chuck allowing to transmit white light through the investigated layer and being collected via an optical fiber which guides the transmitted light into the detection system. For PL measurements, a diode laser (excitation wavelength: 520 nm) excites the sample area under a shallow angle with a laser power density of ~ 75 mW/cm^2. Using this laser power density allows estimating the change in local temperature due to laser heating to be in the range of 0.5 °C (see Supporting Information for details). Resulting PL is collected via the same optical fiber as used for the transmission measurement.

Acknowledgements

S. H., A.K. and Y. Z. acknowledge funding from the Bavarian State Ministry of Science, Research and the Arts for the Collaborative Research Network ‘‘Solar Technologies go Hybrid’’. Y. Z. acknowledges funding from China Scholarship Council. KO.S. acknowledges financial support from the German National Science Foundation (Project KO 3973/2-1 and GRK 1640). M.C., A.K. and F.P. acknowledges support from the Marie Curie Innovative Training Network (ITN) INFORM. We thank the Bavarian Polymer Institute for SEM characterization.

References

1. J. Burschka, N. Pellet, S.-J. Moon, R. Humphry-Baker, P. Gao, M. K. Nazeeruddin and M. Grätzel, *Nature*, 2013, **499**, 316.
2. J.-H. Im, I.-H. Jang, N. Pellet, M. Grätzel and N.-G. Park, *Nature nanotechnology*, 2014, **9**, 927.
3. M. Becker and M. Wark, *Crystal Growth & Design*, 2018, **18**, 4790-4806.
4. Z. Xiao, C. Bi, Y. Shao, Q. Dong, Q. Wang, Y. Yuan, C. Wang, Y. Gao and J. Huang, *Energy & Environmental Science*, 2014, **7**, 2619-2623.
5. H. Chen, *Advanced Functional Materials*, 2017, **27**, 1605654.
6. T.-Y. Hsieh, C.-K. Huang, T.-S. Su, C.-Y. Hong and T.-C. Wei, *ACS applied materials & interfaces*, 2017, **9**, 8623-8633.
7. J. B. Patel, R. L. Milot, A. D. Wright, L. M. Herz and M. B. Johnston, *The Journal of Physical Chemistry Letters*, 2015, **7**, 96-102.
8. D. Barrit, P. Cheng, M.-C. Tang, K. Wang, H. Dang, D.-M. Smilgies, S. Liu, T. D. Anthopoulos, K. Zhao and A. Amassian, *Advanced Functional Materials*, 2019, **29**, 1807544.
9. H. Zhang, J. Mao, H. He, D. Zhang, H. L. Zhu, F. Xie, K. S. Wong, M. Grätzel and W. C. Choy, *Advanced Energy Materials*, 2015, **5**, 1501354.
10. S. Mastroianni, F. Heinz, J.-H. Im, W. Veurman, M. Padilla, M. Schubert, U. Würfel, M. Grätzel, N.-G. Park and A. Hinsch, *Nanoscale*, 2015, **7**, 19653-19662.
11. H. Ko, D. H. Sin, M. Kim and K. Cho, *Chemistry of Materials*, 2017, **29**, 1165-1174.
12. N. Ahn, S. M. Kang, J.-W. Lee, M. Choi and N.-G. Park, *Journal of Materials Chemistry A*, 2015, **3**, 19901-19906.
13. Y. Fu, F. Meng, M. B. Rowley, B. J. Thompson, M. J. Shearer, D. Ma, R. J. Hamers, J. C. Wright and S. Jin, *Journal of the American Chemical Society*, 2015, **137**, 5810-5818.
14. S. Yang, Y. C. Zheng, Y. Hou, X. Chen, Y. Chen, Y. Wang, H. Zhao and H. G. Yang, *Chemistry of Materials*, 2014, **26**, 6705-6710.
15. M. Buchhorn, S. Wedler and F. Panzer, *The Journal of Physical Chemistry A*, 2018, **122**, 9115-9122.
16. S. Singh, C. Li, F. Panzer, K. Narasimhan, A. Graeser, T. P. Gujar, A. Köhler, M. Thelakkat, S. Huettner and D. Kabra, *The Journal of Physical Chemistry Letters*, 2016, **7**, 3014-3021.
17. F. Panzer, S. Baderschneider, T. P. Gujar, T. Unger, S. Bagnich, M. Jakoby, H. Bässler, S. Hüttner, J. Köhler and R. Moos, *Advanced Optical Materials*, 2016, **4**, 917-928.
18. F. Panzer, C. Li, T. Meier, A. Köhler and S. Huettner, *Advanced Energy Materials*, 2017, **7**, 1700286.
19. A. Merdasa, A. Kiligaridis, C. Rehermann, M. Abdi-Jalebi, J. Stöber, B. Louis, M. Gerhard, S. D. Stranks, E. L. Unger and I. G. Scheblykin, *ACS Energy Letters*, 2019, **4**, 1370-1378.
20. J. Li, A. Dobrovolsky, A. Merdasa, E. L. Unger and I. G. Scheblykin, *ACS Omega*, 2018, **3**, 14494-14502.
21. M. Cadelano, M. Saba, N. Sestu, V. Sarritzu, D. Marongiu, F. Chen, R. Piras, F. Quochi, A. Mura and G. Bongiovanni, in *Perovskite Materials-Synthesis, Characterisation, Properties, and Applications*, IntechOpen, 2016.
22. F. Zhang, S. Huang, P. Wang, X. Chen, S. Zhao, Y. Dong and H. Zhong, *Chemistry of Materials*, 2017, **29**, 3793-3799.
23. M. E. Kamminga, H.-H. Fang, M. R. Filip, F. Giustino, J. Baas, G. R. Blake, M. A. Loi and T. T. Palstra, *Chemistry of Materials*, 2016, **28**, 4554-4562.
24. M. Anaya, A. Rubino, T. C. Rojas, J. F. Galisteo‐López, M. E. Calvo and H. Míguez, *Advanced Optical Materials*, 2017, **5**, 1601087.
25. V. Malgras, S. Tominaka, J. W. Ryan, J. Henzie, T. Takei, K. Ohara and Y. Yamauchi, *Journal of the American Chemical Society*, 2016, **138**, 13874-13881.
26. D. N. Dirin, L. Protesescu, D. Trummer, I. V. Kochetygov, S. Yakunin, F. Krumeich, N. P. Stadie and M. V. Kovalenko, *Nano letters*, 2016, **16**, 5866-5874.

27. E. S. Parrott, J. B. Patel, A.-A. Haghighirad, H. J. Snaith, M. B. Johnston and L. M. Herz, *Nanoscale*, 2019, **11**, 14276-14284.
28. L. Polavarapu, B. Nickel, J. Feldmann and A. S. Urban, *Advanced Energy Materials*, 2017, **7**, 1700267.
29. A. Buin, R. Comin, A. H. Ip and E. H. Sargent, *The Journal of Physical Chemistry C*, 2015, **119**, 13965-13971.
30. F. A. Jenkins and H. E. White, *Fundamentals of optics*, Tata McGraw-Hill Education, 1937.
31. J. Manifacier, J. Gasiot and J. Fillard, *Journal of Physics E: Scientific Instruments*, 1976, **9**, 1002.
32. R. Munir, A. D. Sheikh, M. Abdelsamie, H. Hu, L. Yu, K. Zhao, T. Kim, O. E. Tall, R. Li and D. M. Smilgies, *Advanced Materials*, 2017, **29**, 1604113.
33. A. Köhler and H. Bässler, *Electronic processes in organic semiconductors: An introduction*, John Wiley & Sons, 2015.
34. G. Rey, C. Spindler, F. Babbe, W. Rachad, S. Siebentritt, M. Nuys, R. Carius, S. Li and C. Platzer-Björkman, *Physical Review Applied*, 2018, **9**, 064008.
35. C. Prall, C. Kaspari, A. Knauer, K. Haberland, M. Weyers and D. Rueter, *tm-Technisches Messen*, 2017, **84**, 747-752.
36. K. Schötz, M. A. Askar, W. Peng, D. Seeberger, P. T. Guijar, M. Thelakkat, A. Köhler, S. Huettner, M. O. Bakr and K. Shankar, 2019, submitted.
37. T. Yamada, Y. Yamada, Y. Nakaike, A. Wakamiya and Y. Kanemitsu, *Physical Review Applied*, 2017, **7**, 014001.
38. T. Meier, T. P. Gujar, A. Schönleber, S. Olthof, K. Meerholz, S. van Smaalen, F. Panzer, M. Thelakkat and A. Köhler, *Journal of Materials Chemistry C*, 2018, **6**, 7512-7519.
39. T. W. Crothers, R. L. Milot, J. B. Patel, E. S. Parrott, J. Schlipf, P. Müller-Buschbaum, M. B. Johnston and L. M. Herz, *Nano Letters*, 2017, **17**, 5782-5789.
40. J. Schlipf, P. Docampo, C. J. Schaffer, V. Körstgens, L. Bießmann, F. Hanusch, N. Giesbrecht, S. Bernstorff, T. Bein and P. Müller-Buschbaum, *The Journal of Physical Chemistry Letters*, 2015, **6**, 1265-1269.
41. A. E. Lewis, Y. Zhang, P. Gao and M. K. Nazeeruddin, *ACS Applied Materials & Interfaces*, 2017, **9**, 25063-25066.
42. X. Cao, L. Zhi, Y. Jia, Y. Li, K. Zhao, X. Cui, L. Ci, D. Zhuang and J. Wei, *ACS Applied Materials & Interfaces*, 2019, **11**, 7639-7654.
43. Q. Chen, H. Zhou, Z. Hong, S. Luo, H.-S. Duan, H.-H. Wang, Y. Liu, G. Li and Y. Yang, *Journal of the American Chemical Society*, 2013, **136**, 622-625.
44. H. Ko, S. J. Yang, C. Park, D. H. Sin, H. Lee and K. Cho, *ACS Applied Materials & Interfaces*, 2019, **11**, 7037-7045.
45. N. Ahn, D.-Y. Son, I.-H. Jang, S. M. Kang, M. Choi and N.-G. Park, *Journal of the American Chemical Society*, 2015, **137**, 8696-8699.
46. Z.-w. Kwang, C.-W. Chang, T.-Y. Hsieh, T.-C. Wei and S.-Y. Lu, *Electrochimica Acta*, 2018, **266**, 118-129.